Centrifuge modelling of seepage through tailings embankments

Citation for published version:
Beckett, C, Fourie, AB & O'Loughlin, CD 2016, 'Centrifuge modelling of seepage through tailings embankments', *International journal of physical modelling in geotechnics*, vol. 16, no. 1, pp. 18-30. https://doi.org/10.1680/jphmg.14.00045

Digital Object Identifier (DOI):
10.1680/jphmg.14.00045

Link:
Link to publication record in Edinburgh Research Explorer

Document Version:
Peer reviewed version

Published In:
International journal of physical modelling in geotechnics

Centrifuge modelling of seepage through tailings embankments

C.T.S. Beckett[a,], A.B. Fourie[a], C.D. O'Loughlin[b]

[a] *School of Civil, Environmental and Mining Engineering, University of Western Australia, 35 Stirling Highway, Crawley, WA 6009.*
[b] *Centre for Offshore Foundation Systems, University of Western Australia, 35 Stirling Highway, Crawley, WA 6009.*

Abstract

Tailings Storage Facilities (TSFs) are manmade geotechnical structures usually comprising a perimeter embankment, fill material (the tailings) and a water level control system. Key issues often raised in TSF operation are uncertainties surrounding likely seepage to the environment and accurate prediction of seepage surfaces for input into stability assessment. Critically, TSFs are much more complex than current numerical models conventionally assume. This paper presents techniques for investigating steady-state and drawdown seepage behaviour of TSF embankments using a fixed-beam geotechnical centrifuge. The development of experimental equipment for centrifuge testing is described and novel methods to preliminarily characterise model materials, using a "desktop" centrifuge, presented. Good agreement is found between experimental results from the fixed-beam centrifuge and those predicted by the GeoStudio SEEP/W software package for steady-state and drawdown conditions at all tested hydraulic gradients.

Keywords: centrifuge, tailings storage facility, seepage, drawdown

Email addresses: `christopher.beckett@uwa.edu.au` (C.T.S. Beckett), `andy.fourie@uwa.edu.au` (A.B. Fourie), `conleth.oloughlin@uwa.edu.au` (C.D. O'Loughlin)

1. Introduction

It is becoming increasingly difficult to obtain a permit for a new mining operation. One of the abiding concerns is the 'social licence to operate', and key issues often raised in this regard are uncertainty surrounding seepage predictions for Tailings Storage Facilities (TSFs) for input into stability assessment. It might be considered that seepage through a TSF is now a completely tractable problem. However, this is not the case. During tailings deposition, distinct layering often occurs, as shown by numerous piezocone field testing programmes (Williams and Jones, 2005). Some of these layers may be relatively thin, but have a disproportionate effect on the seepage regime (Chang et al., 2011). Furthermore, hydraulic conductivities (k_{sat}) often decrease with depth due to consolidation (Edraki et al., 2014). These effects alone can result in reduced seepage rates to the environment and have sometimes been used as justification for the omission of an underliner.

Use of commercially available software to analyse seepage through TSFs is now relatively commonplace. Elegant pre-processing and finite element mesh refinement techniques are widely available. It is also possible, to a limited extent, to account for heterogeneous tailings parameters, such as anisotropic permeability. The problem remains as to how the relevant parameters may be accurately and routinely measured. It is therefore necessary to generate experimental data that can be used to verify any numerical code, including those that will be produced in the future. There are unfortunately no analytical solutions available for the conditions described above that would enable their verification and calibration.

Geotechnical centrifuge modelling is now a well-established technique for investigating soil behaviour (Madabhushi, 2014). However, relatively few studies have used this technique to investigate seepage phenomena in earthen embankments. Al-Hussaini et al. (1981) presented results for seepage-induced failure of coal-waste embankments, and Cargill and Ko (1983) and Sutherland and Rechard (1984) investigated seepage through homogeneous, trapezoidal earthen embankments to determine phreatic surfaces under steady-state seepage and rapid drawdown of an upstream reservoir. Resnick and Znidarčić (1990) used a similar approach to these works to investigate the influence of horizontal drains on homogeneous slope stability. More recently, Raisinghani and Viswanadham (2011) and Rajabian et al. (2012) employed centrifuge testing to investigate seepage through homogeneous embankments using various geosynthetic reinforcement techniques. These studies all used pressure measurement, digital image correlation (DIC) and/or particle image velocimetry (PIV), to identify total head levels and the position of the phreatic surface during testing. However, all encountered difficulties when comparing experimental results to numerical analyses, due to the creation of complex seepage flow regimes, highlighting inherent challenges in centrifuge testing. This paper presents the development of experimental equipment designed to address these difficulties. Scaling factors necessary for seepage analysis using a geotechnical centrifuge are introduced and the equipment development process described. An experimental programme is then presented for testing steady-state and drawdown seepage flow through a homogeneous embankment, where results are compared to predictions made using the GeoStudio SEEP/W software package (Geo-Slope International). Novel tests for the preliminary material characterisation are also discussed.

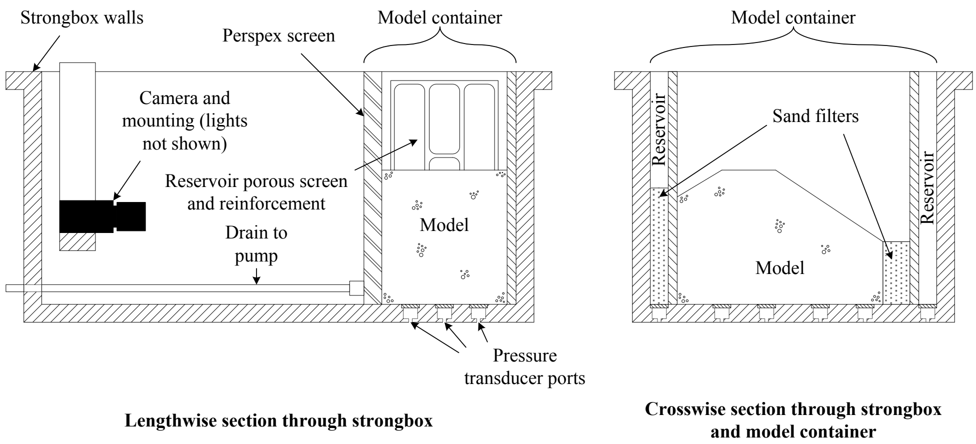

Figure 1: Sectional views through centrifuge strongbox showing principal equipment components and model container

2. Equipment development

2.1. Model container

The equipment used in this investigation was based on that used by Sutherland and Rechard (1984) and Resnick and Znidarčić (1990) comprised a model container housed within a centrifuge “strongbox”, as shown in Figure 1. The assembled strongbox is shown in Figure 2 and an isometric view of the isolated model container in Figure 3.

(Insert Figure 1 somewhere near here)

(Insert Figure 2 somewhere near here)

(Insert Figure 3 somewhere near here)

The model container comprises a central compartment and two flanking reservoirs, separated from the model by porous screens. O-rings were used to prevent seepage around component edges or into the main strongbox. The screens prevent particles from entering the reservoirs whilst allowing water to flow into or out of the model freely. Screens were made from a layer of porous polyethylene

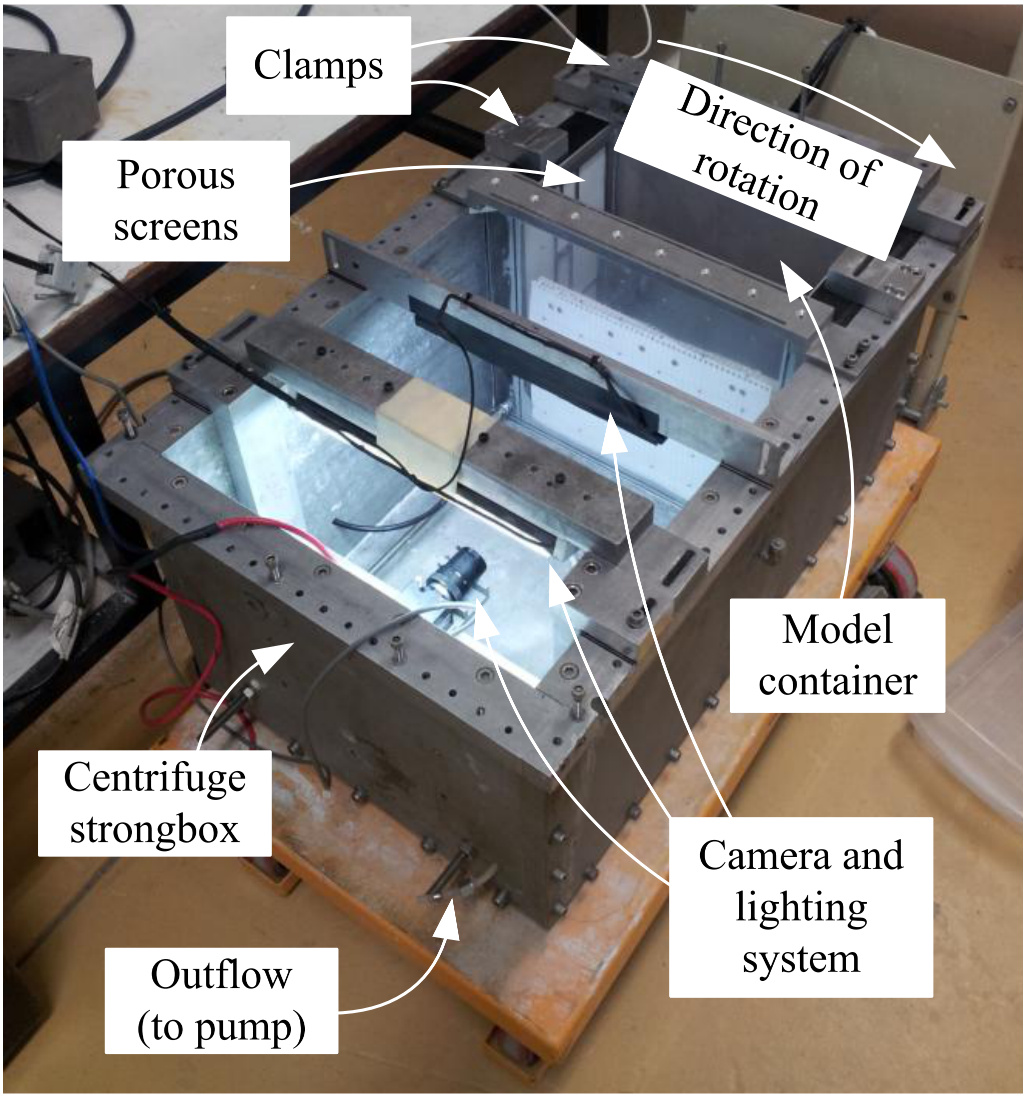

Figure 2: Centrifuge strongbox with installed model container, camera and lighting system

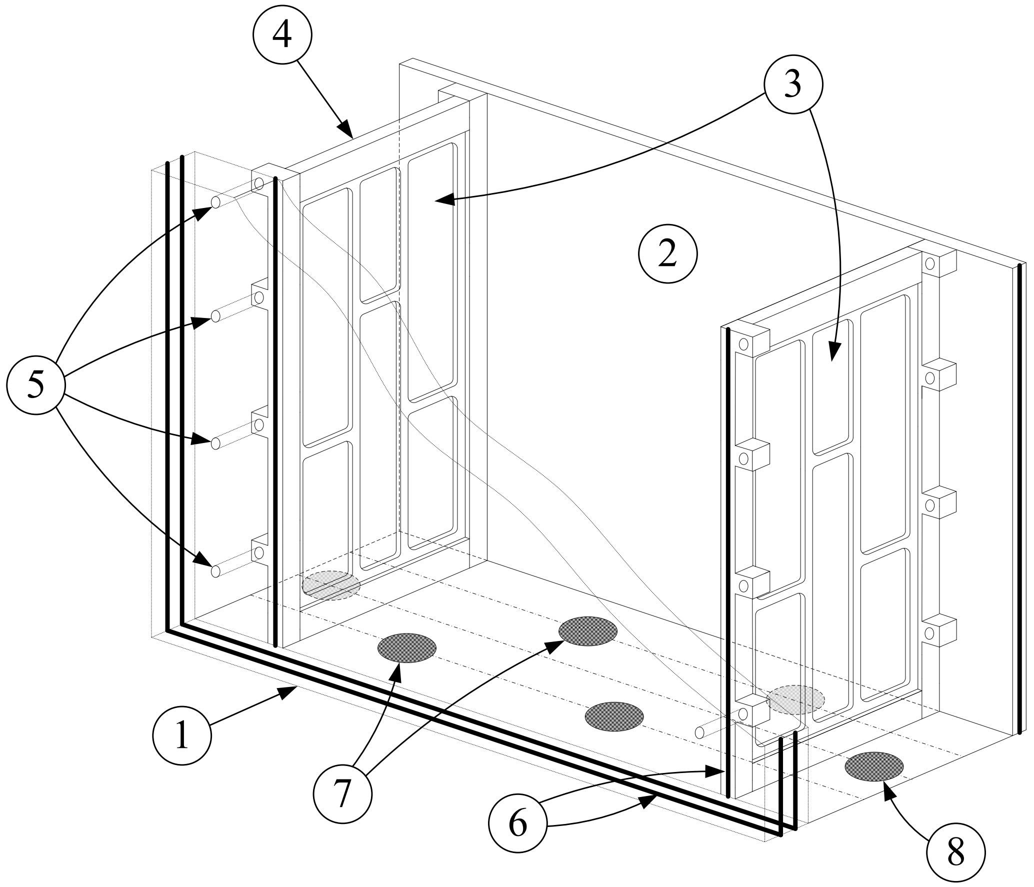

Figure 3: Model container: schematic view and components. 1) Perspex screen; 2) backing plate; 3) porous polyethylene sheets; 4) porous screen frames; 5) bolt holes; 6) O-rings; 7) embankment PPTs (under filters); 8) reservoir PPTs (under filters).

(pore size 35μm), held between a 2mm-thick stainless steel reinforcing grid. An advantage of the use of polyethylene is that sheets can easily be replaced if they become contaminated. The model container was separated from the remainder of the strongbox by a 25mm thick Perspex screen (item 1 in Figure 3), into which markers were embedded to provide a grid of known, fixed coordinates. The use of a Perspex screen allows reservoir fill and phreatic surface levels to be observed during testing. A 5 Megapixel camera (AVT Prosilica GC2450C, Figure 1) was mounted within the strongbox to capture images for future DIC/PIV calculations. The lens can be locked so that the aperture and focus do not unintentionally change in-flight (Stanier and White, 2013).

Pore pressures within the model during testing were measured using four pressure transducers (PPTs), mounted in the strongbox base and protected by Ø25mm sintered bronze filters, as shown in section in Figure 1 and in more detail in Figure 3. PPTs were positioned to lie between the lines of porous screen reinforcement to ensure uninterrupted flow (see Figure 3). PPTs were also installed in the reservoir bases to monitor water levels during testing.

2.2. Pumping system

A number of studies including Sutherland and Rechard (1984) and Resnick and Znidarčić (1990) used overflows in upstream (U/S) and downstream (D/S) reservoirs to control water levels during testing. Flow rates through the model were assumed to equal the flow rate into the U/S reservoir. This is a robust method to ensure consistent water levels, a further advantage of which is that excess water is immediately removed from the centrifuge strongbox, preventing unbalance. However, for mine tailings, consolidation following deposition will result in the expulsion of pore water and so additional (and variable) D/S flow.

Therefore, the simplifying assumption that the rate of injection equals the seepage flow rate is not appropriate.

In this work, D/S water level was maintained by a custom-built syringe pump (internal ∅50mm, 200mm stroke, maximum displacement rate 6.5mm/s, maximum drive pressure 2MPa). The rate of pumping (i.e. the rate of displacement of the syringe) was controlled by an automated process where the syringe actuator was continually adjusted in a closed loop using the analogue signal from the D/S reservoir PPT; if the water level increased, the pumping rate increased to compensate to reestablish the target value. As the stroke and volume of the syringe are known, the flow rate out of the model can easily be calculated from the syringe displacement rate. The use of a pump allowed any D/S water level to be selected; a significant advantage over the use of a fixed overflow, enabling multiple model geometries to be accommodated. The pumping system's hydraulic configuration is shown in Figure 4, where symbols have been selected to be consistent with those used in Shepley and Bolton (2013).

(Insert Figure 4 somewhere near here)

3. Experimental programme

3.1. Model geometry and centrifuge scaling laws

Different scaling factors must be applied to different properties to relate their values in a centrifuge model to those in the full-scale prototype. A summary of similitude laws for centrifuge seepage testing is given in Table 1. For this investigation, geometric and dynamic similarity were achieved by setting $\lambda = \frac{1}{n}$ where λ and n are the length and acceleration ratios between the model and the prototype. A scale factor of $n = 100$ was used for the tests considered here, where

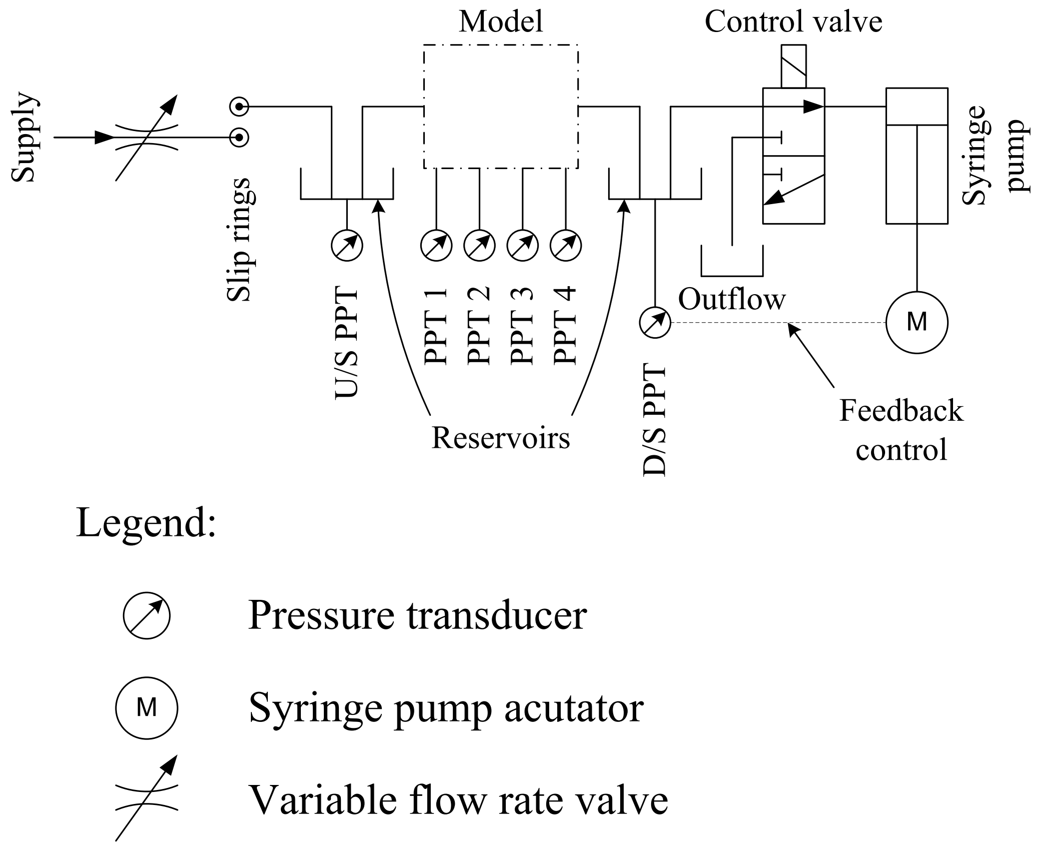

Figure 4: Container hydraulic diagram

Table 1: Summary of scaling factors for centrifuge seepage modelling assuming geometric and dynamic similitude. $X^* = \frac{X_m}{X_p}$ where X_m and X_p are the property vales in the model and prototype respectively. †At steady state

Property	Scaling factor
Model parameters	
Acceleration, g^*	n
Length, λ	$\frac{1}{n}$
Soil parameters	
Angle of friction, ϕ'^*	1
Apparent cohesion, c'^*	1
Soil density, ρ^*	1
Seepage parameters	
Effective stress†, σ'^*	1
Hydraulic conductivity, k^*	1
Hydraulic gradient, i^*	n
Pore pressure†, u^*	1
Seepage velocity, q^*	n
Seepage flow rate, Q^*	$\frac{1}{n}$
Time (kinematic), τ	n
Time (seepage phenomena), t^*	$\frac{1}{n^2}$

n is set at the centre of the model base. This value was used following the work of Al-Hussaini et al. (1981) to avoid potential turbulent seepage flows within the model.

(Insert Table 1 somewhere near here)

The shape chosen for the model was typical of TSF embankments (see Figure 5); a shallow slope was included on the U/S side to represent the tailings pond. It should be noted that the lateral extents of prototype-scale TSFs are much greater than the 37m half-width tested here; a realistic half-width would be of the order of 500m. However, it was necessary to select a truncated profile in order to fit the model within the strongbox whilst testing a sensible range of reservoir head levels.

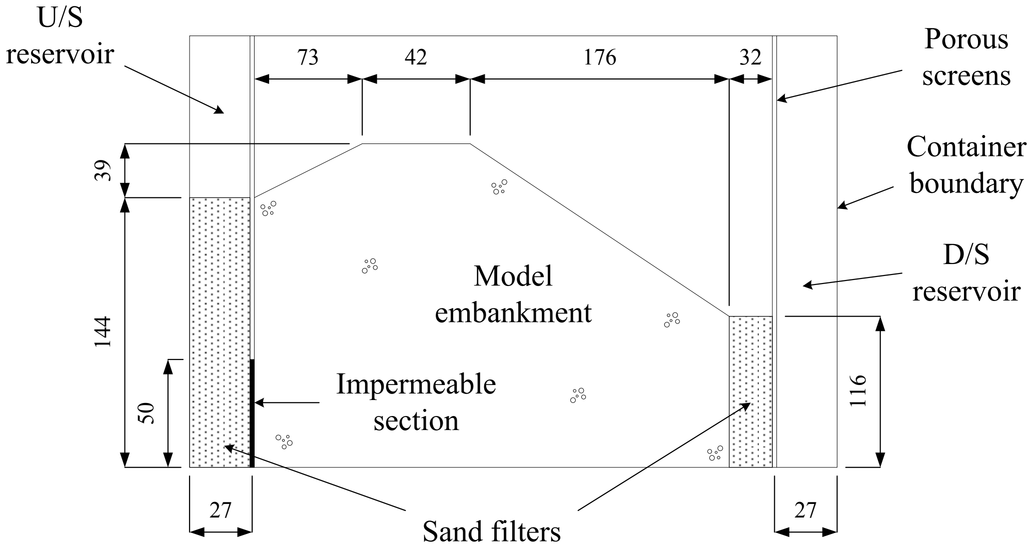

Figure 5: Model dimensions (not to scale)

(Insert Figure 5 somewhere near here)

3.2. Material selection

Although tailings are a distinctly heterogenous material, testing in this investigation was conducted on homogeneous models in order to validate the developed experimental procedures. Silica silt (Unimin Silica 200G) was selected for the main body of the embankment, selected as preliminary testing indicated its hydraulic conductivity to be sufficiently low to keep flow rates within the limits of the pumping system when tested at $n = 100$.

Sand filters (shown in Figures 1 and 5) were used to prevent silt particles migrating into and blocking the porous screens during testing. FEMA (2011) guidelines showed that Unimin RC sand would be a suitable filter material. Silt and sand particle grading curves, as well as the FEMA filter limits, are shown in Figure 6.

(Insert Figure 6 somewhere near here)

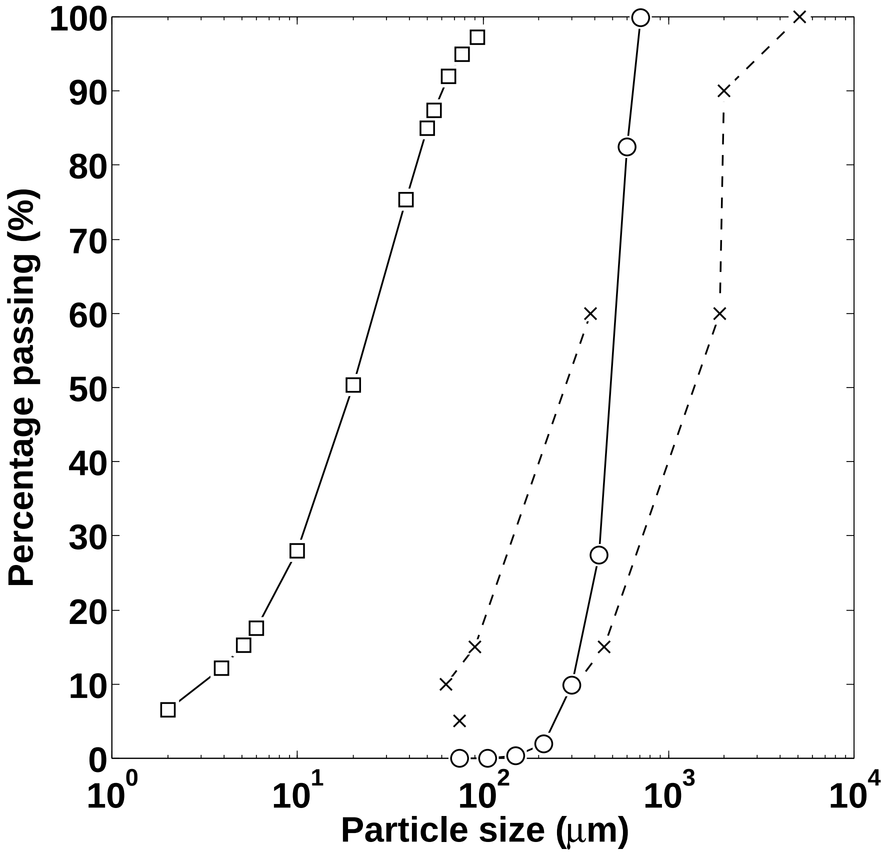

Figure 6: Embankment and filter material particle grading curves. □ RC sand; ○ Silt; × FEMA (2011) filter limits

Table 2: Silt and sand material properties

Property	Symbol	Silt	Sand
Void ratios (-):	e	Figure 8	0.52
	e_{min}	Figure 8	0.47
	e_{max}	Figure 8	0.74
Particle sizes (mm):	d_{10}	0.003	0.299
	d_{60}	0.031	0.496
Specific gravity (-)	G_s	2.65	2.65

(Insert Table 2 somewhere near here)

3.3. Silt consolidation

A small customised desktop centrifuge, shown in Figure 7, was used to determine silt consolidation properties, following the work of Kayabali and Ozdemir (2012) and Reid et al. (2012). The desktop centrifuge is a modified Clements model Orbital 420, commonly used for medical centrifugation. It is equipped with four customised sample canisters, with internal dimensions ∅42mm × 92mm. The desktop centrifuge can spin at speeds of up to 3500RPM, allowing for a maximum acceleration $n = 2400$ at a radius of 175mm, coincident with the base of the canister (Reid et al., 2012). The desktop centrifuge is sufficiently small to be operated for extended periods without the need for specialised facilities. The advantage of this technique over a typical oedometer or Rowe cell is that multiple effective stress states can be examined in a single sample, due to the variation in n with rotation radius.

(Insert Figure 7 somewhere near here)

Consolidation behaviour of the silt was determined by accelerating four samples of silt slurry (at approximately 100% water content by mass) with initial sample heights of 72mm to $n = 100$ (at the canister base) for 24 hours. A customised reaming tool (Reid et al., 2012) was used to remove 2mm slices of consolidated material at specific depths (and so effective stress levels), which were then oven dried to determine their water contents and void ratios. Results are shown in Figure 8. Note that only results for two of the four tested samples are shown in Figure 8 for clarity. Silt void ratios reach a minimum value of 0.7 for effective stresses above 3kPa, indicating that the majority of the silt forming the model embankment is of homogeneous void ratio and so permeability. Such

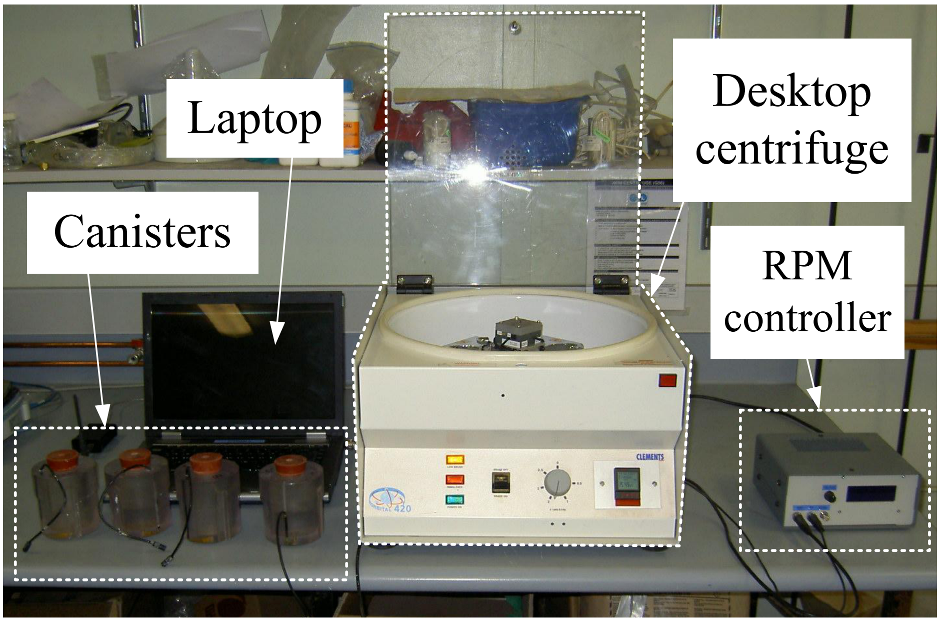

Figure 7: Desktop centrifuge with laptop, customised containers and RPM controller

behaviour is associated with a maximum packing density for the silt particles due to its largely uniform particle size (Figure 6).

(Insert Figure 8 somewhere near here)

3.4. Filter integrity: Desktop centrifuge and image analysis

Given the importance of the sand filters to porous screen integrity, it was necessary to test the ability of the sand filters (Figure 5) to prevent fine particle migration. Testing was conducted using the desktop centrifuge. Centrifuge canisters were filled with a layer of silt slurry, poured over a layer of RC sand. Canisters were then accelerated to $n = 100$ for a period of 7 days, allowing silt to migrate into the underlying sand under gravity. Whilst it is acknowledged that there is no seepage flow in the canister, migration is still possible due to the varying gravitation field.

The reaming tool could not be used to determine the extent of silt migration into the sand as it was not possible to obtain incremental samples from the sand layer. An image-based technique was therefore devised to non-intrusively examine the extent of silt migration, a summary of which is shown in Figure 9. Images of the side wall of each canister were taken from a fixed distance using an 8 Megapixel digital camera. An identically-sized section, corresponding to the interface region between the materials, was then cropped from each image (150×300 pixels). The variation in pixel intensity in each of the red, blue and green channels was then analysed. To account for any changes in lighting conditions between samples, pixel intensities were normalised using

$$I' = \frac{I - I_{min}}{I_{max} - I_{min}} \tag{1}$$

where I_{max} and I_{min} are the maximum and minimum intensities found in the

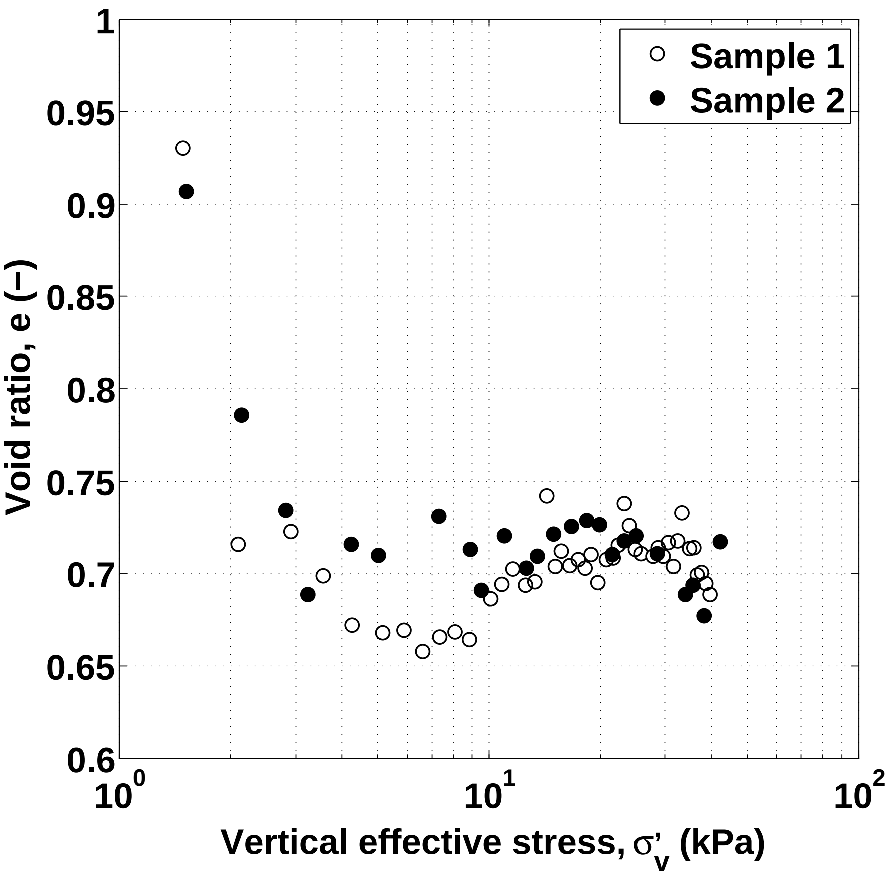

Figure 8: Silt consolidation as determined using the desktop centrifuge

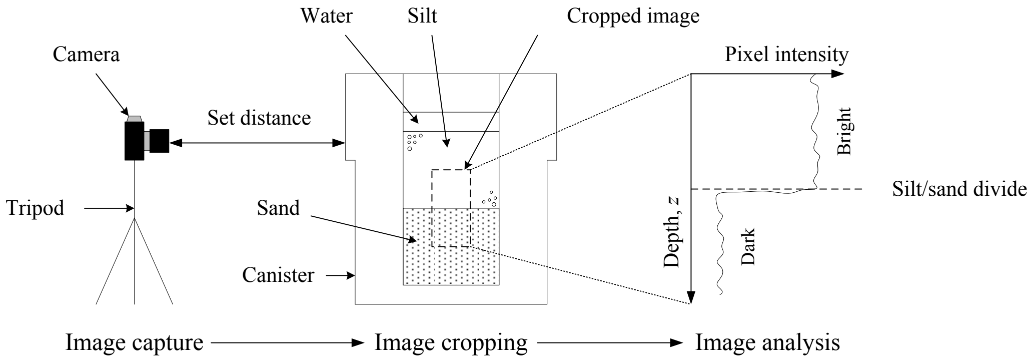

Figure 9: Process used for filter integrity testing

image and I' is the normalised pixel intensity value. Using Eqn 1, the brightest pixel intensities (i.e. white) equal 1 whist the darkest (i.e. black) equal 0.

(Insert Figure 9 somewhere near here)

Results for four tested silt-sand samples are shown in Figure 10, where depths have been determined directly from the captured images. Note that results in Figure 10 are for the blue channel only, as this provided the greatest contrast between materials. A clear discontinuity in pixel intensity is visible between depths of 19 to 25mm, corresponding to the transition between lighter silt and darker sand particles. Also evident in Figure 10 is an increase in pixel intensity from 0 to 19mm. Although darker intensities might suggest the presence of sand, this feature is instead due to shadowing from the canisters' rims; no sand was found above the layer interface. The transition depth of 6mm between the two materials in Figure 10 suggests that a minimum filter width of 6mm is required to prevent particle migration. Given that seepage flow was not present in the desktop centrifuge canisters, a final filter thickness of 32mm was selected to ensure that the porous screens remained uncontaminated.

(Insert Figure 10 somewhere near here)

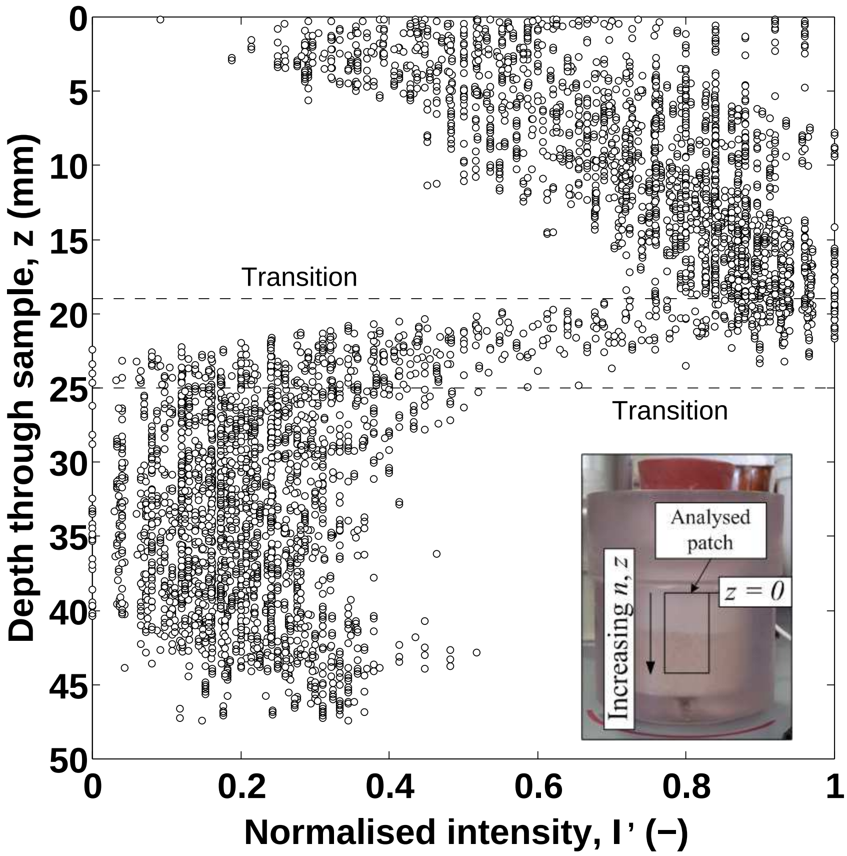

Figure 10: Normalised pixel intensities against depth (results for every 10^{th} pixel only for clarity). Inset: Example photograph showing analysed cropped image section.

3.5. Model construction

The embankment and toe filter were constructed by pouring silt slurry (roughly 30% water content by mass) and dry sand either side of a temporary plastic divider. Dry sand was deposited at a relative density of 90% by pluviation through air. U/S and D/S reservoir water levels were maintained above those of the fill during construction to prevent seepage from the model into the U/S reservoir (which might cause blockage) and to saturate the sand filter. Sand was also poured into the U/S reservoir to act as a support for the porous screen during testing. Sand was not used in the D/S reservoir to avoid migration of particles into the pumping system. The plastic divider was slowly removed once the fill reached the required depth, and water levels increased to inundate the entire model. The model was then consolidated in the centrifuge at $n = 100$ for 24 hours, after which the water level was reduced and the embankment formed by profiling the silt to create the required geometry (Figure 5).

3.6. Steady-state seepage and drawdown testing

Steady-state seepage conditions are representative of those present in the TSF embankment during normal operations, where tailings are deposited as a slurry within the facility and water levels are controlled by the ponding systems. Steady-state seepage testing was conducted by selecting a constant D/S reservoir level (at a depth below the surface of the sand filter) and raising the U/S reservoir water level above that value. The U/S reservoir water level was maintained at that level until steady-state seepage conditions were achieved (as demonstrated by the container PPTs), a process that took approximately 2 hours. The U/S water level was then increased to the next testing value. This process was repeated until ponding was observed on the U/S embankment slope. Flow to the U/S reservoir was then terminated and water levels allowed to reduce until equilibrium was re-established with the D/S reservoir level, simulating reservoir "drawdown" at the closure of a TSF. The entire testing cycle was then repeated for a different set of target U/S reservoir water levels.

4. Head level calculations

4.1. PPT responses

The pore pressure response for one complete testing cycle (i.e. a series of U/S reservoir height increases followed by drawdown) are shown in Figure 11. An example extracted section of these data, corresponding to a period of steady-state seepage, is shown in Figure 12, where linear regression lines have been added to the data to demonstrate that steady-state conditions were achieved. It is noted that regressions fitted to measured PPT responses have negligible, rather than zero, gradients. However, pressure gradients in Figure 12 correspond to pressure variations of no greater than 0.25kPa over the 100s period, so that conditions were effectively steady-state.

Due to the use of a syringe pump, a series of spikes can be seen in the PPT responses shown in Figure 11. These are due to the emptying of the pump via the outflow (Figure 4), which resulted in a temporary increase in the D/S reservoir water level. Hence, spikes decrease in severity with distance from the D/S reservoir and increase in magnitude with increasing hydraulic gradients due to higher flow rates. Care was therefore taken to avoid emptying the pump towards the end of an equilibration period, to prevent erroneous readings. A large spike is seen in Figure 11 at roughly 7600s; this was due to an error in the operation of the control valve (Figure 4), resulting in the pump drawing

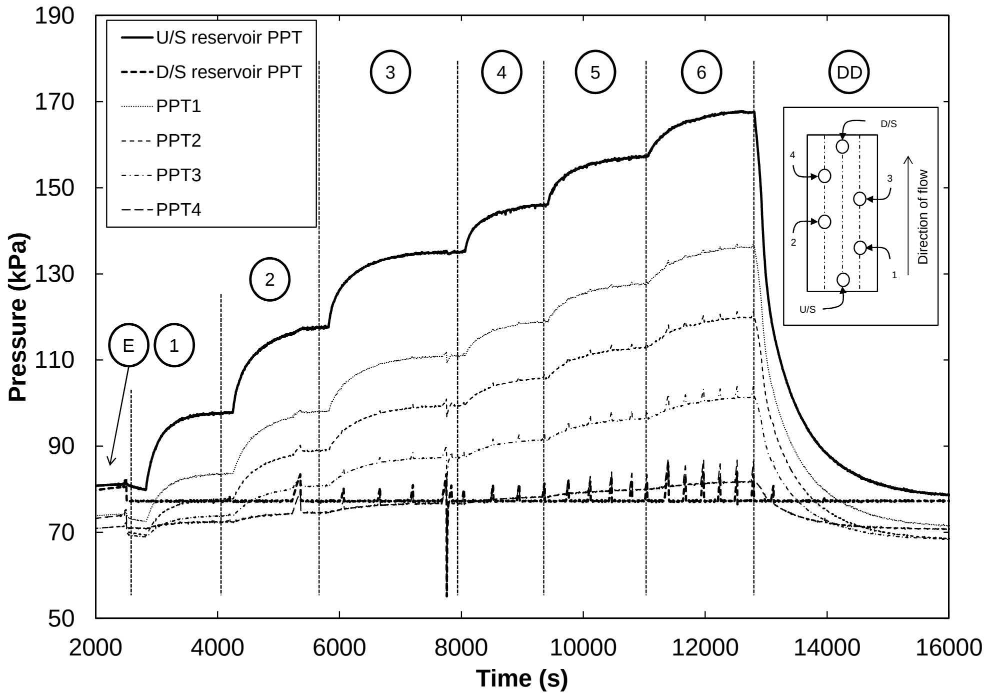

Figure 11: PPT measurements obtained during one full test cycle: E) initial equilibration; 1-6) steady-state flow equilibration periods; DD) U/S reservoir drawdown. Inset: PPT numbering and direction of flow.

additional water from the D/S reservoir after emptying. With the exception of these spikes, Figure 11 shows that the syringe pump provided excellent control over the D/S water levels for the duration of the test. This system can therefore be used to control more complicated seepage regimes in heterogeneous materials, e.g. tailings.

(Insert Figure 11 somewhere near here)

(Insert Figure 12 somewhere near here)

4.2. Calculation of equivalent head levels

Two corrections are required to determine the position of the prototype phreatic surface from model head levels, h_m:

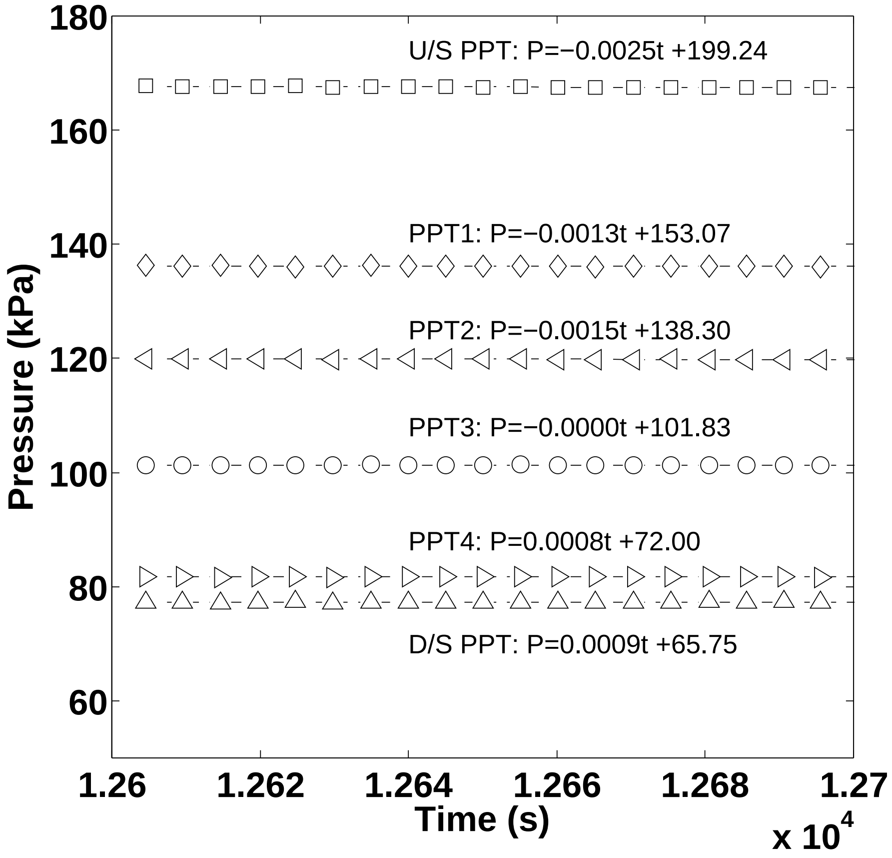

Figure 12: Example extracted PPT pressure measurements (P) against time (t) at steady state (data and PPT numbering as per Figure 11)

- Correction for the centrifuge's radial gravitation field; PPTs detect the pressure at the base of a water column with an axis that extends from the point of measurement towards the centrifuge hub, rather than vertically upwards.

- Correction for the average gravity acting on the water column; the gravitational field varies linearly with radius from the centrifuge hub, so that the average gravity acting on the water column also varies with its length.

Total model head can be calculated from measured PPT pressures, P, via

$$h_m = \frac{P}{\rho_w n_{av} g} \tag{2}$$

where ρ_w is the density of water at the testing temperature, g is the acceleration due to Earth's gravity (i.e. 9.81 m/s^2) and n_{av} is the average acceleration scale factor for the water column. As n varies linearly with radius from the centrifuge hub, n_{av} is found from the average of the n values at the bottom and top of the water column:

$$n_{bottom} = n\left(\frac{r}{R}\right) \tag{3}$$

$$n_{top} = n\left(\frac{r - h_m}{R}\right) \tag{4}$$

$$n_{av} = \frac{n}{2}\left(\frac{2r - h_m}{R}\right) \tag{5}$$

where r is the radius from the centre of rotation to the PPT location and R is the radius from the hub to the base of the model along its centreline, as shown in Figure 13. For Eqns 4 to 5, $n = 100$ at $R = 1760$mm (i.e. the distance from the centre of rotation to the model base along its centreline, as shown in Figure

13). Equivalent non-radial head, H_m, can then be determined via

$$H_m = h_m - (r - R) \tag{6}$$

Given the non-vertical orientation of the water column, the length-wise coordinate of the top of the water column (i.e. the predicted location of the phreatic surface), X_m, must also be determined from the PPT lengthwise coordinate, x_m, via

$$X_m = (x_m \pm \Delta x_m) = \left(x_m \pm h_m \sin\left(\text{arccos}\left(\frac{R}{r}\right)\right)\right) \tag{7}$$

where Δx_m is additive or subtractive depending on whether the PPT lies to the left or right of the centreline. Eqns 2 to 7 relate measured pressures to the equivalent total head at the model centreline. Hence, prototype head level, h_p, and corresponding lengthwise coordinate of the phreatic surface, x_p, can then be found via $h_p = nH_m$ and $x_p = nX_m$.

(Insert Figure 13 somewhere near here)

5. Steady-state behaviour

The software package GeoStudio 2007 SEEP/W was used to predict prototype performance, given calculated prototype U/S and D/S reservoir water levels and scaling laws provided in Table 1. Experimental and predicted results for total head levels are shown in Figures 14. Note that, as PPTs are mounted in the model container base, predicted results shown in Figure 14 are those calculated at the mesh base nodes. A comparison of experimental results and those found at these nodes is shown in Figure 15.

Figures 14 to 15 show good agreement between measured and predicted head

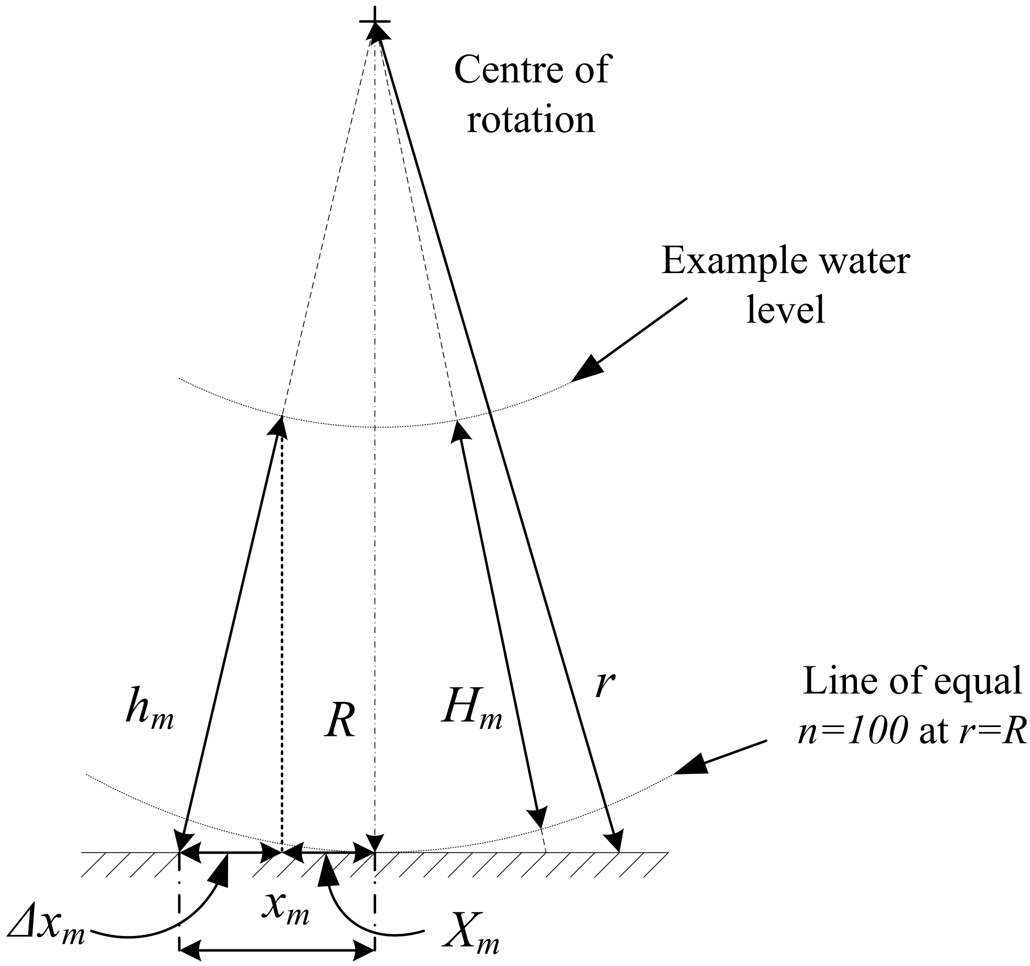

Figure 13: Conversion between model and equivalent prototype head levels.

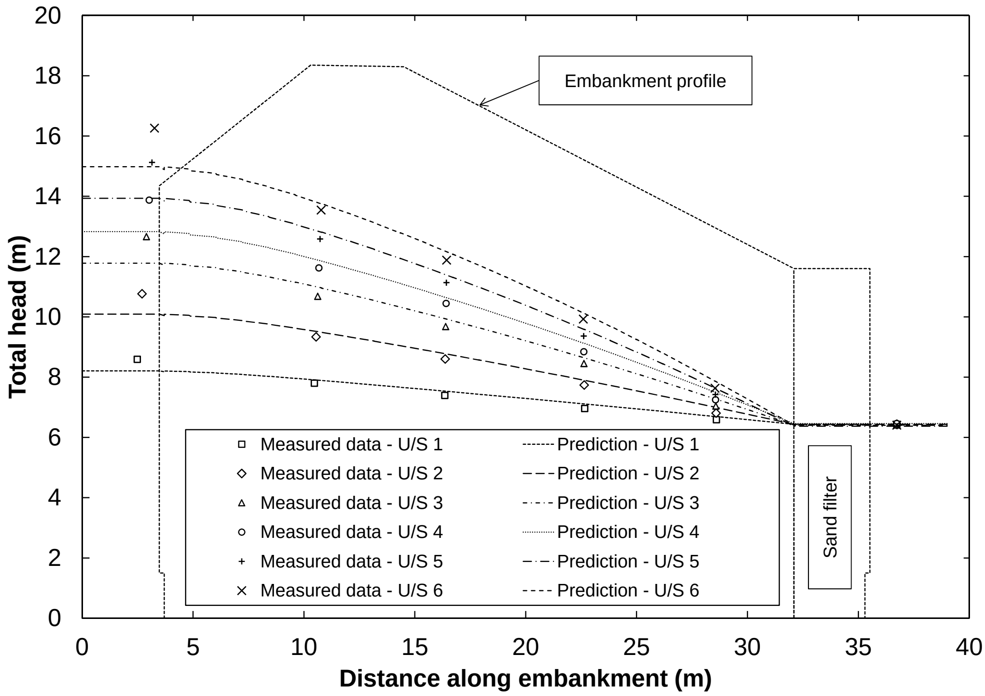

Figure 14: Example Predicted and measured results for steady-state seepage. Legend numbers correspond to U/S head increase periods shown in Figure 11.

values, as demonstrated in Figure 15 by results falling on or near to the line of equality. Although it might be expected that errors would be a function of the imposed hydraulic gradient, Figure 15 suggests that an upper error limit of 0.3m exists for all measured head levels. It is therefore likely that this error is due to the simplifying assumptions made in the numerical analysis, for example that no significant head drop occurred across the U/S porous screen.

(Insert Figure 14 somewhere near here)

(Insert Figure 15 somewhere near here)

Notably, Figure 14 shows that predicted U/S head levels are consistently lower (by much more than 0.3m) than those measured in the U/S reservoir. This is unexpected, as U/S reservoir water levels were used as a boundary condition

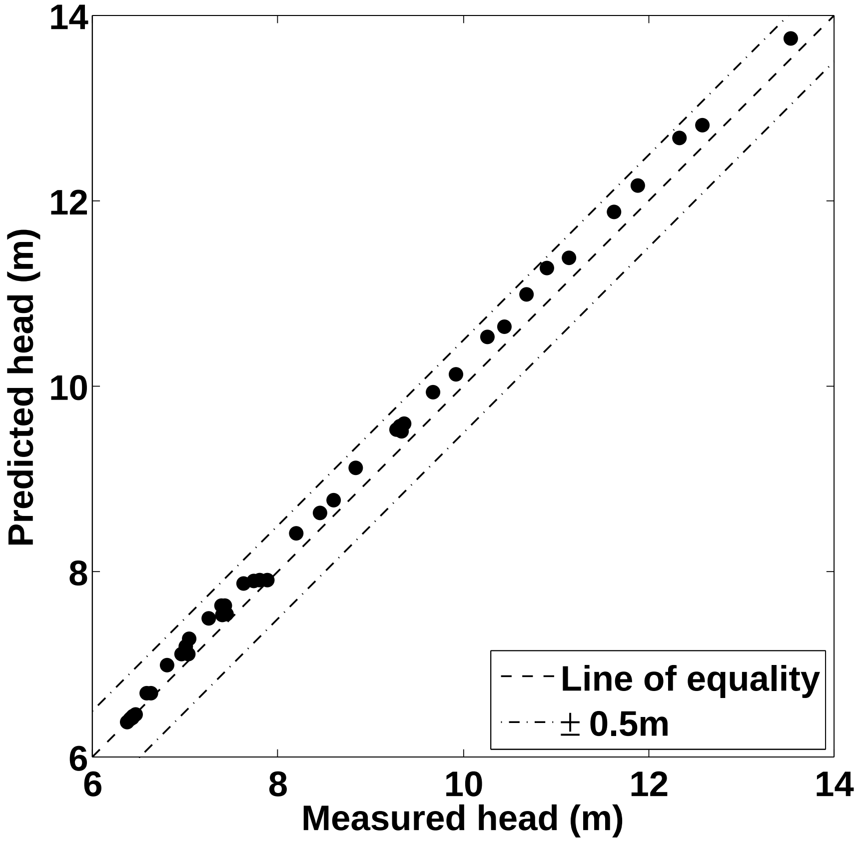

Figure 15: Predicted against measured steady-state embankment head levels for all U/S head levels (not including U/S reservoir elevations)

in the numerical analysis. A similar error is not seen for D/S reservoir levels, also used as a boundary condition; predicted and measured D/S head levels match. Figure 16 compares measured and predicted head levels as obtained from SEEP/W for PPT results given in Figure 12. Figure 16 shows that the predicted SEEP/W phreatic surface agrees with measured U/S and D/S values, as expected. However, the inclusion of a short impermeable section in the U/S porous screen, shown in Figure 5, results in the distortion of the equipotential lines so that they are not perpendicular to the model base. Hence, the full total head range is not detected by the base-mounted PPTs. Although a deep embankment base was used to attempt to elevate flow above this restriction, it is clear from Figure 16 that insufficient clearance was provided. A similar issue was experienced by Raisinghani and Viswanadham (2011) due to the presence of layers of geosynthetics. It is clearly essential, therefore, that seepage phenomena investigated using this technique are designed so that flow is, as far as practicable, parallel to the model base. Provided that these issues are accommodated, results shown in Figures 14 to 15 demonstrate that the experimental approach developed in this investigation can accurately reproduce steady-state seepage conditions within homogeneous embankments.

(Insert Figure 16 somewhere near here)

6. Drawdown behaviour

Drawdown of the U/S reservoir was modelled using transient seepage analysis in SEEP/W. Steady-state analyses were used to establish the phreatic surface, after which a reducing head boundary condition was applied to the U/S face of the reservoir, whilst maintaining a constant head level at the D/S model face. The reduction in U/S head level with time was determined directly from mea-

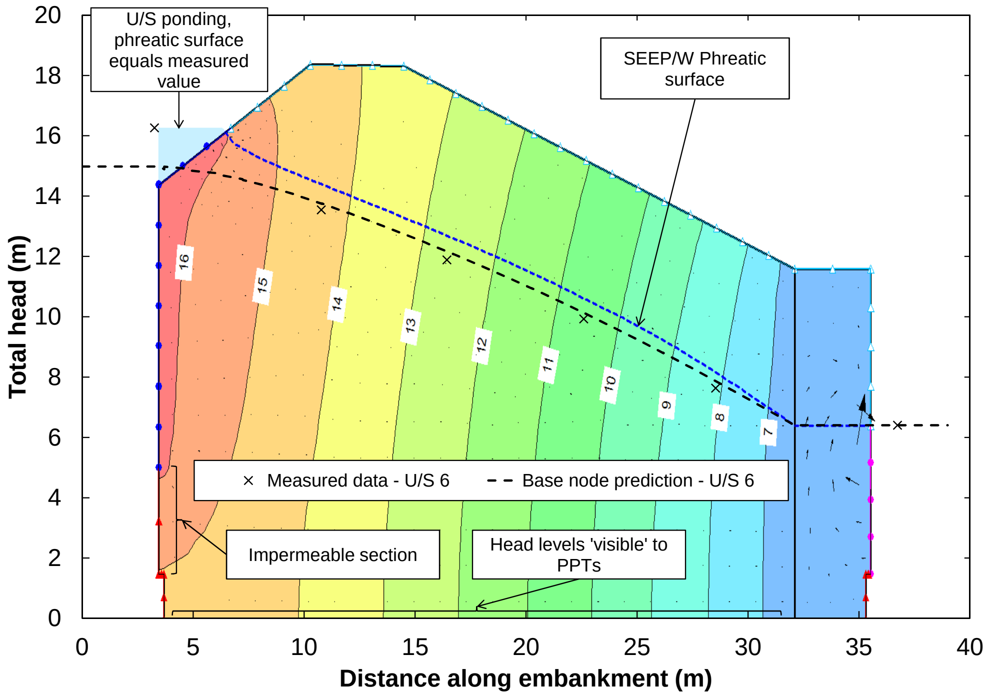

Figure 16: SEEP/W analysis for data given in Figure 12 compared to measured values (equipotential values given in m)

sured data for the U/S PPT, as shown in Figure 11, using an analysis period of $3.5{\times}10^7$s.

As transient seepage modelling was used, estimates for material retention and hydraulic properties were required. Initial estimates for material water retention curves for silt and sand are shown in Figure 17, based on data provided in Fredlund and Xing (1994) and known values of e (Table 2). Estimates for k_{sat} were obtained using

$$k_{sat}(\text{cm/s}) = C_0 \frac{\mu_0}{\mu_T} \left(\frac{n - 0.13}{\sqrt[3]{1-n}} \right)^2 d_{10}^2 \qquad (8)$$

where $C_0 = 8$ for smooth particles, $\frac{\mu 0}{\mu_T} = 1.3$ for testing at 20°C, $n = \frac{e}{1+e}$ and e and d_{10} (in mm for use with Eqn 8) are as given in Table 2 (Terzaghi, 1925). It should be noted that the transient phreatic surface experiences increasing accelerations, and so increasing values of k_{sat}, as its level reduces. However, as this change is small for small changes in elevation, analyses were conducted assuming $n = 100$ for all head levels.

(Insert Figure 17 somewhere near here)

Although drawdown is a transient phenomenon, negligible difference was found between analyses for variations in k_{sat} of several orders of magnitude, due to the experimentally-defined U/S boundary condition. Seepage was therefore suggestibly sufficiently slow to be largely independent of hydraulic properties (i.e. quasi-static). Initial estimates for retention and hydraulic properties were therefore deemed sufficient for comparison to experimental data. Note that, for heterogeneous materials such as mine tailings, this simplification would not be valid and accurate retention and hydraulic conductivity functions would be required.

Figure 18 shows example experimental and predicted results for total head

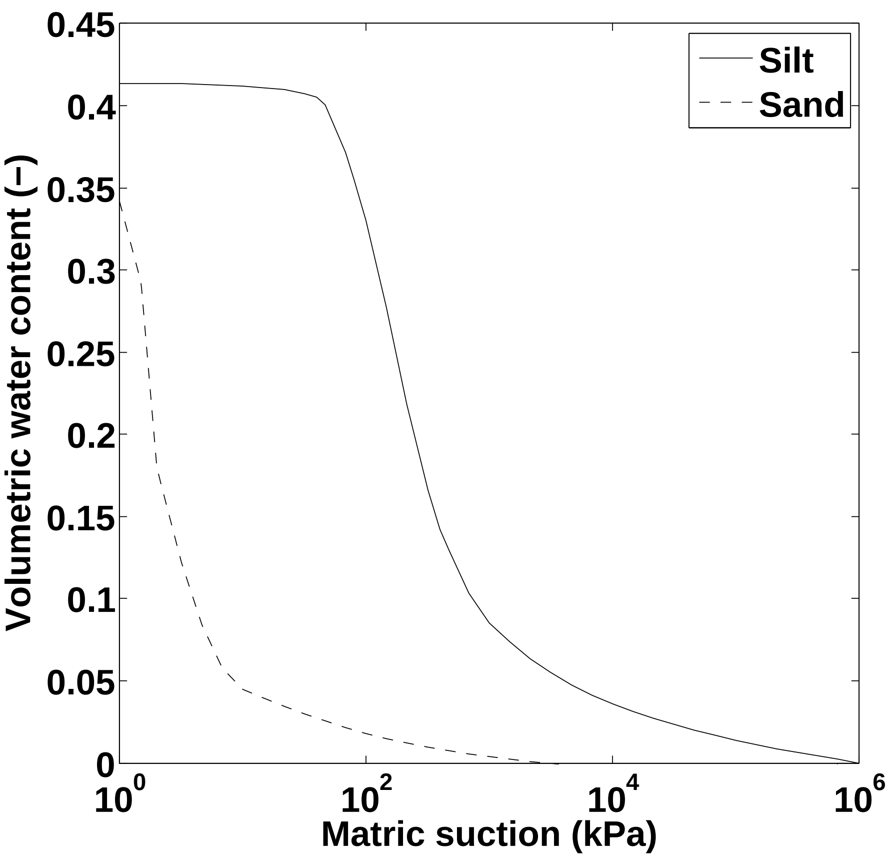

Figure 17: Estimated soil-water retention curves for silt and sand

levels (predicted at the embankment base) during drawdown. Predicted and experimental values are compared in Figure 19. Good agreement is seen in Figure 18 between measured and predicted results throughout the embankment profile. This is also shown in Figure 19, where errors are within ±0.4m and fall evenly about the line of equality. Drawdown was largely complete after 3200s, equivalent to roughly 370 days at $n = 100$. As discussed previously, however, the larger lateral extents of full-scale TSFs mean that drawdown times in practice are likely to be far longer than those found in this work, suggesting that pumping might be required for decades in order to fully restore groundwater equilibrium.

Unlike in Figure 15, both positive and negative differences are seen in Figure 19. A potential cause of this error is the assumption that $n = 100$ at all times during drawdown. Overprediction of processes dominated by horizontal flow (i.e. steady-state seepage surfaces) and underprediction of those dominated by vertical flow (i.e. reducing head levels during transient seepage) also suggests that a degree of heterogeneity existed within the embankment material, so that $k_{sat,h} > k_{sat,v}$. This is consistent with the deposition of the silt slurry in layers during model construction; although material was subsequently consolidated, preferential flow in the horizontal direction may have remained. This is an important observation, as it is well-known that layered structures are also created during tailings deposition in TSFs. Scale models should therefore incorporate this layered structure in order to capture the effects of hydraulic heterogeneity on seepage performance.

(Insert Figure 18 somewhere near here)

(Insert Figure 19 somewhere near here)

The good agreement found between measured and predicted steady-state and drawdown results demonstrates that experimental techniques developed and em-

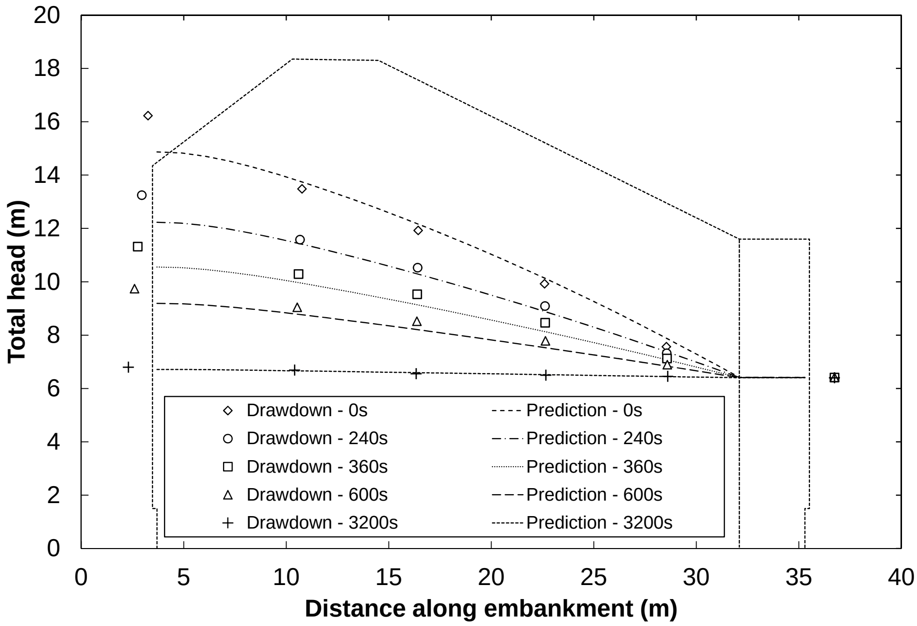

Figure 18: Example predicted and measured results for times following U/S reservoir drawdown.

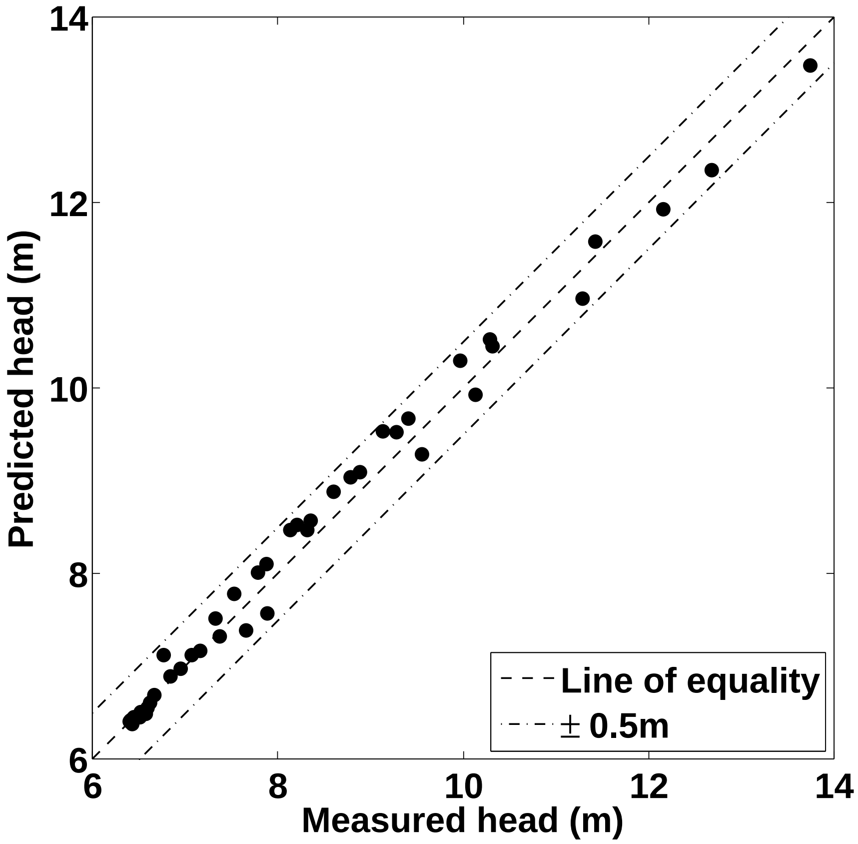

Figure 19: Predicted against measured steady-state embankment head levels for all U/S head levels during drawdown (not including U/S values)

ployed in this investigation are able to accurately capture embankment seepage behaviour. Notably, these techniques offer greater flexibility than those previously used in terms of D/S flow rate measurement and accurate control of U/S and D/S water levels. This facility can now be used to investigate more complicated seepage scenarios, for example those encountered in full-scale TSFs, to provide data for improving current seepage prediction models.

7. Conclusion

Seepage conditions within TSF embankments are likely to be far more complicated than current models predict. There is therefore a need for experimental data against which updated numerical models can be verified. This paper has described the design and development of apparatus for measuring seepage through model TSF embankments using a geotechnical centrifuge. The use of a syringe pump was shown to be an effective method to control D/S water levels and to measure seepage flow rates. Novel processes for determining material consolidation behaviour and sand filter effectiveness using a desktop centrifuge and image-based analysis were also described, each providing rapid alternatives to conventional testing methods.

Results for steady-state seepage through a homogeneous model were presented and good agreement was found between measured results and those predicted for an equivalent full-scale prototype using SEEP/W. A maximum error of 0.3m was found between measured and predicted results, which was seemingly independent of testing hydraulic gradient and attributed to assumptions made during numerical modelling. It was also demonstrated that flow through the model must be designed so that it is parallel to the model base if seepage behaviour is to be tested using equipment similar to that developed in this work.

Predicted results for changes in total head during U/S reservoir drawdown, based on simplifying quasi-steady assumptions, showed good agreement with numerical predictions. Differences of ± 0.4m between measured and predicted values were similar to those found for steady-state seepage. A comparison of steady-state and drawdown experimental results suggested that these differences were due to a slight material heterogeneity developed during deposition. A drawdown time of roughly 370 days was predicted for the tested embankment profile. Based on these results, there is confidence that techniques developed here can reliably reproduce seepage conditions within full-scale heterogeneous embankments.

8. Acknowledgements

The authors would like to gratefully acknowledge funding awarded from The Integrated Tailings Management Project, funded through AMIRA International by; Anglo American, Freeport McMoran, Gold Fields, Total E&P Canada, Newmont, Shell Canada Energy, BASF, Nalco and Outotec.

9. References

Al-Hussaini, M. M., Goodings, D. J., Schofield, A. N., Townsend, F. C., 1981. Centrifuge modeling of coal waste embankments. Journal of the Geotechnical Engineering Division 107, 481–499.

Cargill, K., Ko, H., 1983. Centrifugal modeling of transient water flow. J. Geotech. Engrg. 109 (4), 536–555.

Chang, N., Heymann, G., Clayton, C., 2011. The effect of fabric on the behaviour of gold tailings. Géotechnique 61, 187–197.

Edraki, M., Baumgartl, T., Manlapig, E., Bradshaw, D., Franks, D. M., Moran, C. J., 2014. Designing mine tailings for better environmental, social and economic outcomes: a review of alternative approaches. Journal of Cleaner Production in press.

FEMA, 2011. Filters for embankment dams: Best practices for design and construction. Tech. rep., Federal Emergency Management Agency.

Fredlund, D. G., Xing, A., 1994. Equations for the soil-water characteristic curve. Canadian Geotechnical Journal 31, 521–532.

Kayabali, K., Ozdemir, A., 2012. Assessing the practicality of the centrifuge method for 1-d consolidation. Bulletin of Engineering Geology and the Environment 71 (4), 735–745.

Madabhushi, G., 2014. Centrifuge modelling for civil engineers. CRC Press, UK.

Raisinghani, D., Viswanadham, B., 2011. Centrifuge model study on low permeable slope reinforced by hybrid geosynthetics. Geotextiles and Geomembranes 29, 567–580.

Rajabian, A., Viswanadham, B., Ghiassian, H., Salehzadeh, H., 2012. Centrifuge model studies on anchored geosynthetic slopes for coastal shore protection. Geotextiles and Geomembranes 34, 144–157.

Reid, D., Fourie, A., Watson, S., 16–19 April 2012. Accelerated consolidation testing of slurries using a desktop centrifuge. In: Jewell, R., Fourie, A., Paterson, A. (Eds.), Proceedings of the 15th International Seminar on Paste and Thickened Tailings (PASTE 2012). Australian Centre for Geomechanics, Sun City, South Africa, pp. 43–52.

Resnick, G. S., Znidarčić, D., 1990. Centrifugal modeling of drains for slope stabilization. Journal of Geotechnical Engineering 116 (11), 1607–1624.

Shepley, P., Bolton, M. D., 2013. Water supply to a geotechnical centrifuge. International Journal of Physical Modelling in Geotechnics 13, 99–110.

Stanier, S. A., White, D. J., 2013. Improved image-based deformation measurement in the centrifuge environment. Geotechnical Testing Journal 36, 1–14.

Sutherland, H., Rechard, R., 1984. Centrifuge simulations of stable tailings dam. J. Geotech. Engrg. 110 (3), 390–402.

Terzaghi, K., 1925. Principles of soil mechanics. Engineering News Records 95 (19, 742–746; 20, 796–800; 21, 832–836; 22, 874–878; 23, 912–915; 25, 987–990; 26, 1026–1029; 27, 1064–1068).

Williams, D., Jones, H., 2005. Tailings storage facilities. In: Wills, B. A. (Ed.), Advances in Gold Ore Processing. Vol. 15 of Developments in Mineral Processing. Elsevier, Amsterdam, The Netherlands, Ch. 30, pp. 729–752.

Figure captions:

1. Sectional views through centrifuge strongbox showing principal equipment components and model container
2. Centrifuge strongbox with installed model container, camera and lighting system
3. Model container: schematic view and components. 1) Perspex screen; 2) backing plate; 3) porous polyethylene sheets; 4) porous screen frames; 5) bolt holes; 6) O-rings; 7) embankment PPTs (under filters); 8) reservoir PPTs (under filters).
4. Container hydraulic diagram
5. Model dimensions (not to scale)
6. Embankment and filter material particle grading curves. □ RC sand; ○ Silt; × FEMA (2011) filter limits
7. Desktop centrifuge with laptop, customised containers and RPM controller
8. Silt consolidation as determined using the desktop centrifuge
9. Process used for filter integrity testing
10. Normalised pixel intensities against depth (results for every 10^{th} pixel only for clarity). Inset: Example photograph showing analysed cropped image section.
11. PPT measurements obtained during one full test cycle: E) initial equilibration; 1-6) steady-state flow equilibration periods; DD) U/S reservoir drawdown. Inset: PPT numbering and direction of flow.
12. Example extracted PPT pressure measurements (P) against time (t) at steady state (data and PPT numbering as per Figure 11)
13. Conversion between model and equivalent prototype head levels.

14. Example Predicted and measured results for steady-state seepage. Legend numbers correspond to U/S head increase periods shown in Figure 11.
15. Predicted against measured steady-state embankment head levels for all U/S head levels (not including U/S reservoir elevations)
16. SEEP/W analysis for data given in Figure 12 compared to measured values (equipotential values given in m)
17. Estimated soil-water retention curves for silt and sand
18. Example predicted and measured results for times following U/S reservoir drawdown.
19. Predicted against measured steady-state embankment head levels for all U/S head levels during drawdown (not including U/S values)

Table captions:

1. Summary of scaling factors for centrifuge seepage modelling assuming geometric and dynamic similitude. $X^* = \frac{X_m}{X_p}$ where X_m and X_p are the property vales in the model and prototype respectively. †At steady state
2. Silt and sand material properties